PHYSICAL REVIEW E VOLUME 61, NUMBER 4 APRIL 2000

Extensive experimental mapping of sonoluminescence parameter space

Jeffrey A. Ketterling* and Robert E. Apfel
Department of Mechanical Engineering, Yale University, New Haven, Connecticut 06520

(Received 29 September 1999)

Experimental phase diagrams are compared to theoretical predictions based on the Dissociation Hypothesis (DH) theory of single bubble sonoluminescence (SBSL). Ambient radius (R_o)- acoustic drive pressure (P_a) phase diagrams are presented for krypton-nitrogen mixtures and for a collection of data with other noble gas-nitrogen mixtures. The data is also presented in terms of expansion ratio (maximum bubble radius R_{max}/R_o) vs P_a and relative light intensity vs P_a. The results provide further evidence of the validity of DH and also provide a thorough mapping of SBSL at a single frequency.

PACS number(s): 78.60.Mq, 43.25.+y

I. INTRODUCTION

Bubbles with an ambient radius (R_o) on the order of 5 μm can be acoustically levitated in a time varying acoustic field [$P(t)=-P_a\cos(\omega t)$]. When the acoustic drive pressure (P_a) is ≈ 1.3 atm, the bubble grows to a maximum radius (R_{max}) of ≈ 50 μm and upon its violent collapse, it gives off a pulse of light. This process is known as single bubble sonoluminescence (SBSL) [1]. One of the particularly interesting early observations relating to SBSL was that the presence of a noble gas was required for there to be any significant light emission [2].

The observations of Hiller *et al.* [2] along with some additional theoretical work [3] and experimental results [4], helped to support what is commonly referred to as the Dissociation Hypothesis (DH) [5–7]. DH permits predictions of bubble behavior in R_o-P_a parameter space based on the concentrations of gases dissolved in the fluid. These predictions and their theoretical basis have been thoroughly described elsewhere [5–7] and have been shown to be consistent with experimental results [7–10].

Briefly, when a bubble is luminescing, the noble gas concentration determines where in parameter space the bubble is stable. Before luminescing, a bubble can also reach a stable dissociation equilibrium that is determined by the partial pressure of the diatomic gas present in the fluid. Outside of these regions, the bubble displays unstable behavior, causing it to break up, dissolve, or undergo a repeated pinch off and growth process.

Expansion ratio (ER, $=R_{max}/R_o$) vs P_a diagrams provide an additional parameter space to examine experimental data in the context of DH. Unlike R_o-P_a phase diagrams, ER gives information about the energy concentration at bubble collapse. Gaitan and Holt [8] were the first to study the ER from a single experimental case and correlate it to the light emission. What they observed was quite surprising. While the number of photons emitted increased as P_a increased, the ER actually *decreased*, which seems to contradict earlier observations [11] and calculations [12]. However, the observations of Gaitan and Holt are in fact consistent with theory when the path of a single gas saturation is followed in parameter space, as Moss *et al.* [13] have recently shown.

Gaitan and Holt also noted the ratio of light intensity to bubble volume decreased as the light intensity increased. This implies that energy concentration is greater for higher ER's even though the absolute light intensity is lower and that a higher ER does not necessarily mean more photons are emitted. The emitting volume of the bubble and to some extent the contents of the bubble also need to be considered.

In this paper, experimental R_o-P_a and ER-P_a phase diagram results are presented and compared to theoretical predictions based on DH. These results expand on previous experimental work [4,8,9]. Phase diagrams were obtained for mixtures of helium-nitrogen, neon-nitrogen, argon-nitrogen, krypton-nitrogen, xenon-nitrogen, pure helium, pure argon, pure nitrogen, helium-argon-nitrogen, neon-argon-nitrogen, and air [10]. However, only the results for the krypton-nitrogen mixtures and the overall collection of data are presented here. Relative light intensity vs P_a data is also shown.

II. APPARATUS

The test cell used for all experiments was a cylindrical quartz crystal cell (76 mm diameter, 74 mm height) with brass endcaps that was acoustically driven by a ceramic piezoelectric transducer attached to the bottom brass endcap [9,10]. The construction of the cell allowed it to be fully evacuated. Each brass endcap had a Swagelok® QC series quick release fitting that allowed the cell to be coupled to an external gas-handling and fluid preparation system. A fluid sample was first prepared in this external system before being transferred to the test cell. By using an input and output line, fluid could be transferred to the cell without exposing the fluid to air or changing the gas pressure above the fluid.

Bubble levitation was accomplished by tuning the test cell to a resonant mode at ≈ 32.8 kHz and selecting a P_a at which a bubble could be trapped. An air filled syringe needle was then inserted into the cell via a small opening in the top, allowing a bubble to be seeded from the gas trapped on the needle tip. Air was *not* injected, which would have led to unknown quantities of air being introduced into the fluid and to gas bubbles accumulating at the top of the cell.

Once fluid had been transferred to the cell, the cell was moved to a holding bracket that held it fixed relative to two

---

*Present address: Riverside Research Institute, 330 W. 42nd St., New York, NY 10036.

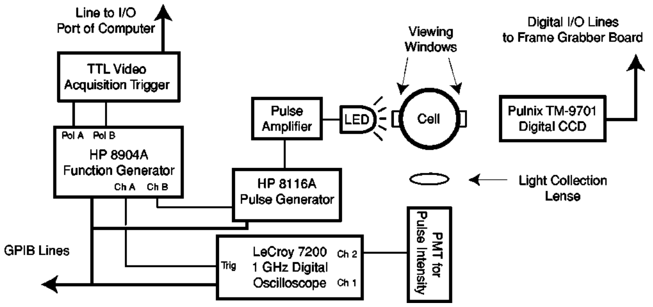

FIG. 1. Schematic of diagnostic instrumentation.

diagnostic tools: a stroboscopic imaging system (SIS) to measure the bubble radius and a photomultiplier tube (PMT) to measure the relative intensity of the light pulse. The various components of the system were mounted to an optical bench to allow precise positioning with translation stages and to avoid realignment for each new experiment. A schematic of the overall diagnostic set up will be referred to as each of the diagnostic tools are discussed (Fig. 1).

The SIS is very similar to the one constructed by Tian *et al.* [14] but with a slightly higher magnification. It was also similar to the optics set up used by Holt and Gaitan [4,8] but their strobe rate was chosen to match the capture rate of their video camera (1/60 s) rather than slaved to a signal slightly offset (-0.1 Hz) from the drive frequency.

The SIS consisted of a homemade microscope with a charge-coupled device (CCD) attached to its viewing end and a light emitting diode to strobe the bubble. The CCD (Pulnix TM-9701) output was fed directly into a computer containing an Epix® PIXCI-D™ digital frame grabbing card allowing real time video acquisition. Each video acquisition commenced on the same phase of the drive signal, by using an external circuit to trigger the Epix® PIXCI-D™.

Using the SIS as described above, it was thus possible to acquire time-averaged movies of a bubble oscillation. After acquiring a bubble oscillation image sequence, the images could be analyzed to extract a time averaged radius-time history $R(t)$ of the bubble (Fig. 1 of Ref. [9]). From the $R(t)$ curve three key parameters were extracted: R_{max} (± 1.1 μm), R_o (± 0.9 μm), and P_a (± 0.07 atm). R_{max} was just the maximum radius value measured for the $R(t)$ curve. R_o was chosen from the $R(t)$ curve based on the definition of R_o in the Rayleigh-Plesset (RP) equation. R_{max} and R_o were then used to infer P_a using the RP equation [9].

Relative SL intensity

The components used to measure the SL light intensity are shown in Fig. 1. The light pulse was detected with a PMT, and the signal was captured with a LeCroy 7200 digital oscilloscope. A collection lens (6 cm diameter and focal length) was fixed at the end of a tube attached to the PMT housing. The bubble was located at the focal point of the collection lens.

To measure the relative light intensity of SL, the peak value of the light pulse needs to be determined. However, the peak value can be hard to determine from a single pulse, since small changes in bubble dynamics can lead to fairly large changes in the SL intensity either from pulse to pulse or over several seconds [3,15,16]. For these reasons, the LeCroy's built-in histogram functions were used to measure the relative intensity.

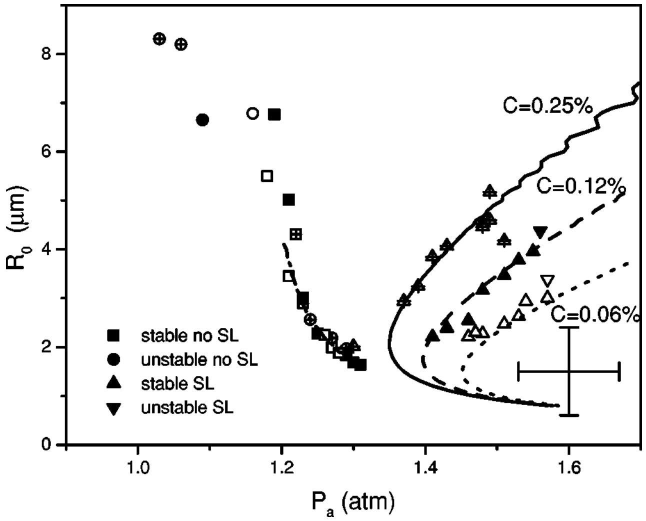

FIG. 2. Phase diagram of 1% krypton- 99% nitrogen mixture saturated to $C=5\%$ (open symbols), 10% (solid symbols), and 20% (open symbols with + inside). Stable diffusive equilibrium curves are shown for $C=0.06\%$ (dotted), $C=0.12\%$ (dashed), and $C=0.25\%$ (solid). The stable dissociation equilibrium for a 10% air saturation calculated by Arlman is also shown (dash dotted). The crosshairs represent the experimental error.

By using the histogram functions, the peak value for thousands of pulses could be accumulated and assembled into a histogram. Normal settings were 20 mV for the bin width and greater than 1000 for the sample size, although several hundred samples were usually enough to determine the highest occurring SL light pulse value. An interesting feature seen occasionally in the light pulse histograms was the occurrence of two distinct peaks. To our knowledge, this observation has not been directly reported in the literature. However, Holt *et al.* [15] have observed similar behavior, but their measurements focused more on the time separation between SL flashes.

III. RESULTS AND DISCUSSION

A. Krypton R_o vs P_a phase diagram

Of all the noble gases, krypton has been the least studied in SL experiments. Some emission spectra have been measured by Barber *et al.*, [11] but little other information exists. Krypton, therefore, makes an interesting case study.

Figure 2 shows the R_o vs P_a phase diagram for a single 1% krypton and 99% nitrogen mixture saturated to $C=5\%$ (open symbols), $C=10\%$ (solid symbols), and $C=20\%$ (open symbols with + inside). Each data point represents data from a single $R(t)$ curve. Each experimental run is represented by a different symbol type (open, solid, and open with + inside) and is further broken down into four types of behavior: stable non-SL (square), unstable non-SL (circle), stable SL (upward pointing triangle), and unstable SL (downward pointing triangle).

Cases were considered unstable if the bubble showed signs of ''dancing'' [1,4,17] or excessive drift during video acquisition. Dancing behavior usually indicated that the bubble was near a shape mode threshold [4,5,18,19]. The unstable cases included in the phase diagrams remained on the video monitor long enough to obtain a full $R(t)$ curve, although the bubble may have moved off screen for some video frames. For cases where the bubble ''danced,'' the bubble was imaged at the largest R_o that it grew to before pinching off and then growing back in size. The location of the unstable bubbles in parameter space was very consistent from run to run, indicating that their video acquisition was reliable.

The curves shown in the plot represent diffusive equilibrium curves for a fixed gas concentration C computed at $f = 33$ kHz using the Eller-Flynn formulation [20]. A positive slope represents diffusive stability. Bubbles to the right of a curve tend to grow by rectified diffusion while bubbles to the left tend to dissolve [3,6,20]. Also shown is the curve representing the stable dissociation equilibrium for 10% air (dash dotted) calculated by Arlman *et al.* [21].

The actual amount of krypton appears slightly higher than expected, and the data is therefore compared to the apparent concentration of the noble gas rather than the predicted concentration. The stable SL points (upward pointing triangles) from the $C = 5\%$ run are shown relative to the $C = 0.06\%$ curve (dotted), the points from the $C = 10\%$ run to the $C = 0.12\%$ curve (dashed), and the points from the $C = 20\%$ run to the $C = 0.25\%$ curve (solid). The agreement between the stable SL data and the calculated C curves is exactly what DH predicts as is that between the stable non-SL data and the dissociation equilibrium.

This case highlights some features of stable SL behavior for decreasing noble gas partial pressures. First, the P_a where SL turns on increases as the partial pressure decreases. This behavior arises because the point where the slope of the C curves turns positive occurs at higher P_a as C decreases. Second, the P_a where SL turns off also increases as C decreases. Finally, the R_o where SL turns off decreases with decreasing C. These final two effects result from the C curves and the extinction threshold (not shown) intersecting at lower R_o and higher P_a as C decreases [5]. What causes the sudden extinction is not well understood [22].

B. Krypton light intensity vs P_a diagram

The light intensity diagram vs P_a for krypton is shown in Fig. 3. The light emission for each saturation seems to follow a distinct path with the larger saturations following a steeper path and reaching a higher maximum intensity. The lines marked with a C value are meant to illustrate the separate paths and are not theoretical calculations. The light intensity at a fixed P_a is not the same for the different saturations. Similar behavior was seen for mixtures of xenon and nitrogen, but was not observed for mixtures containing helium, neon, or argon in nitrogen. For these cases, large differences in light intensity were not observed as the noble gas saturation levels varied [10].

The difference in light emission can be understood in terms of diffusive stability. As C increases for a fixed P_a, the number of atoms inside a bubble increases for two reasons. First, Henry's law states that the amount of gas saturated in a fluid is proportional to the pressure of the gas above the fluid ($C_\infty \propto p_\infty$). Clearly, for the bubble to remain in equilibrium for C_∞, its time averaged internal gas pressure $\langle p(t) \rangle_4$ must be equal to p_∞ (Eq. 36 of Ref. [5]). Thus, as C increases, the pressure inside the bubble also increases and, according to the ideal gas law, the number of atoms in the bubble also increases if we assume the volume is fixed.

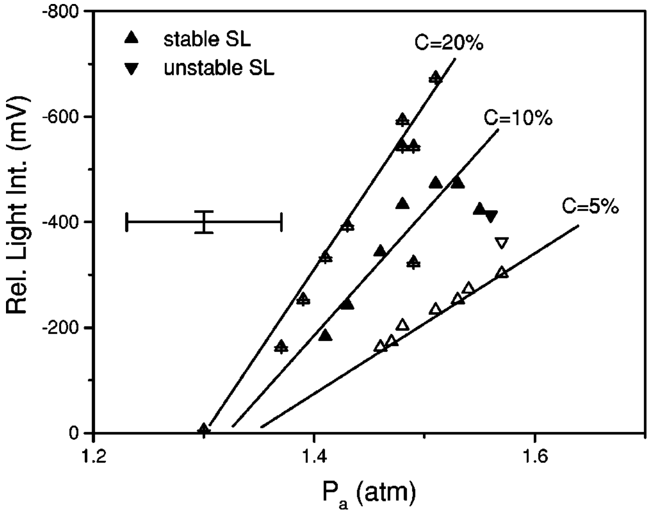

FIG. 3. Relative light intensity diagram of 1% krypton- 99% nitrogen mixture saturated to $C = 5\%$ (open symbols), 10% (solid symbols), and 20% (open symbols with + inside). The curves for each concentration indicate the separate paths the light emission follows for each saturation and are not theoretical calculations.

The second reason that the number of atoms increases in a bubble is because R_o increases as C increases for a fixed P_a. Again, using the ideal gas law, an increase in R_o means an increase in bubble volume, and thus an increase in the number of atoms if we assume pressure is fixed. The cases with a higher C are, therefore, brighter because they have more atoms that can emit due to an increase in bubble volume and in time-averaged pressure. However, since the bubble dynamics for each case are not the same, this description oversimplifies the observations, and it is helpful to examine the ER for the experimental data.

C. Krypton ER vs P_a diagram

The ER vs P_a diagram for krypton (Fig. 4) helps clarify the relationship between ER and light emission. Plotted in the figure are the respective ER curves calculated from the krypton diffusive equilibrium curves of $C = 0.06\%$ (dotted), $C = 0.125\%$ (dashed), $C = 0.25\%$ (solid). Two features of the data are apparent: the ER for a single run decreases with increasing P_a, and the ER also decreases for increasing krypton concentration.

Referring back to the intensity diagram (Fig. 3) reveals an interesting correlation between the light emission and ER. Each run is brighter as P_a increases, and the higher krypton saturation cases are brighter than the lower ones for a fixed P_a. Thus, a higher ER leads to a lower light emission: a prime example of the need to draw a distinction between energy focusing (energy per unit radiating volume) and light emission [8]. The greatest energy focusing occurs at SL turn-on for the $C = 5\%$ run which is also the highest ER (≈ 17). The greatest light emission occurs at the SL turn-off for the $C = 20\%$ cases which is the lowest ER (≈ 10).

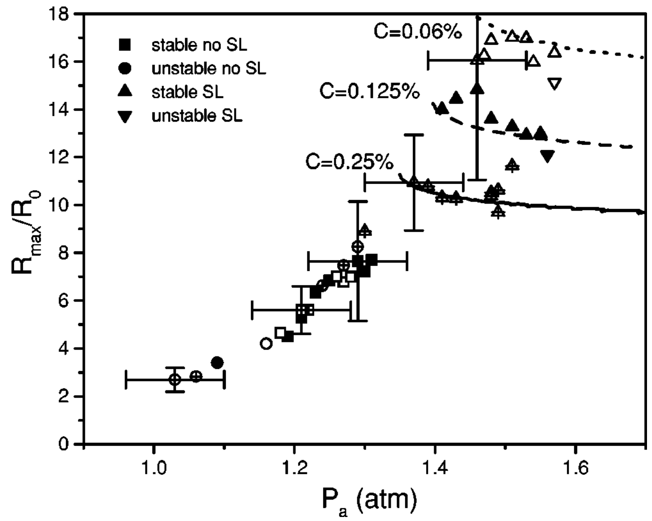

FIG. 4. Expansion ratio diagram of 1% krypton- 99% nitrogen mixture saturated to $C=5\%$ (open symbols), 10% (solid symbols), and 20% (open symbols with + inside). ER curves calculated from their respective diffusive equilibrium curves are shown for $C=0.06\%$ (dotted), $C=0.125\%$ (dashed), $C=0.25\%$ (solid).

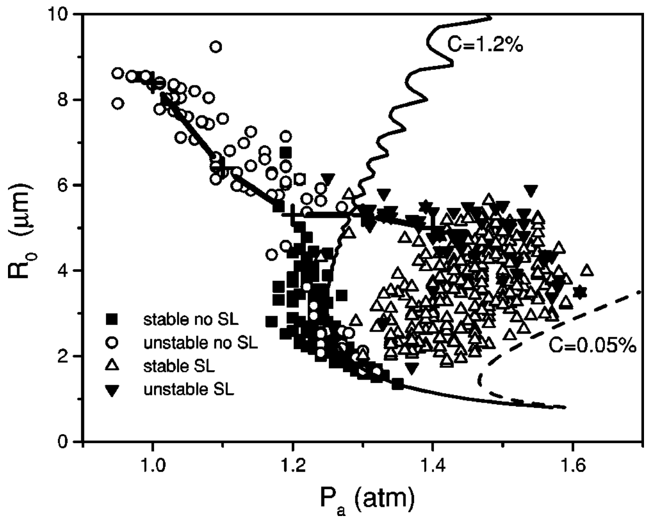

FIG. 5. Phase diagram with data points from numerous experimental runs at an assortment of gas saturations. Diffusive equilibrium curves are plotted for $C=1.2\%$ (solid) and $C=0.05\%$ (dashed). The $n=4$ shape threshold (solid with +) calculated by Wu is also shown.

The reason for light emission differences as C varied for a single noble gas mixture was discussed earlier, but without including the ER. Including ER tends to confuse the matter, though, because it needs to be considered in relation to the number of emitting atoms in the bubble. Bubbles with smaller ER have a larger R_o and C and thus contain more atoms inside. Even though the energy concentration decreases, the larger number of emitters makes up for the relatively small number of photons emitted, and the bubble appears bright. Likewise, bubbles with high ER have a lower R_o and C and contain fewer emitters. While the total number of photons per emitter increases, the increase is not enough to make the bubble appear brighter than for the low ER case. Obviously, a balance can be reached where two bubbles emit the same light but with a different ER and different number of emitting atoms, as can be seen in Fig. 3. This simplified discussion leaves out issues such as opacity [7,13] and the quenching effect of water vapor inside the collapsing bubble [13,23], which also play a role in the observed differences between cases. These effects have been included in recent SL models to successfully reproduce experimental results such as the spectral features and duration of the SL pulse [7,13].

D. Overall R_o vs P_a phase diagram

When the parameter space data from all our experimental runs are plotted together, the result is the phase diagram shown in Fig. 5. The unstable non-SL bubbles (open circles) occur at higher C and lower P_a where there is only unstable diffusive equilibria. Unstable SL (solid triangles) was seen to agree fairly well with the $n=4$ shape threshold (solid with +) calculated by Wu [24] at 33 kHz using the method described in Ref. [18]. Unstable non-SL behavior also showed agreement with the $n=4$ mode, but because the $n=2,3,4$ modes lie close together for low P_a (Fig. 1 of Ref. [25]), the lower order modes are just as likely the cause of unstable behavior for lower P_a [4].

The stable non-SL bubbles (solid squares) represent a stable dissociation equilibrium reached as the nitrogen dissociated each cycle equals the amount of nitrogen entering the bubble by rectified diffusion. The data shows that the range of R_o for stable non-SL decreases as P_a increases. The region appears to show more variation for a fixed P_a and changing nitrogen content than indicated by the present calculations [21].

The region where stable SL (open triangles) is observed shows remarkable agreement with the predictions of DH. The region is roughly bounded on the left by $C=1.2\%$ (solid) and on the right by $C=0.05\%$ (dashed), although a lower concentration may be the true bound on the right. Between these two curves are a plethora of stable concentration curves that the bubbles can follow. The lower bound of the SL region is the point on the concentration curves where the slope becomes positive. The upper bound of SL is marked by the $n=4$ shape threshold, which an unstable bubble appears to travel along as P_a increases, and which may also act as the SL extinction threshold for higher P_a (>1.45 atm) [5,25].

E. Overall light intensity vs P_a diagram

Figure 6 shows a compilation of the light intensity vs P_a data from all the phase diagrams. The paths of the light intensities for a 1% xenon-99% nitrogen mixture saturated to $C=20\%$ and $C=5\%$ are indicated in the diagram, since they seem to provide the bounds for all the light intensity data. These two concentrations are not the absolute bounds, but merely the highest and lowest xenon concentrations for which data was collected. Why xenon represents the lowest and highest intensities at a fixed P_a is not clear.

Figure 6 is mainly useful in showing that most of the data falls roughly together, with the $C=20\%$ xenon case being the main standout. The data also shows that the range of P_a where SL occurs increases as the light level increases. A more extended set of experiments would likely reveal more about the light emission trends.

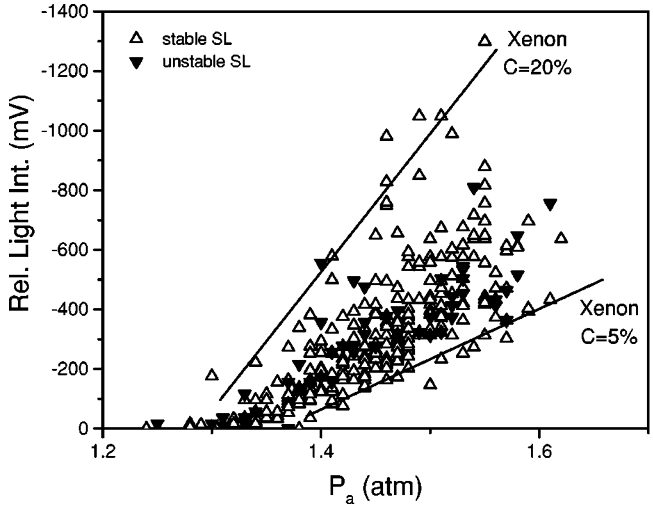

FIG. 6. Relative light intensity diagram with data points from numerous experimental runs at an assortment of gas saturations. The data is bounded by experimental runs with 1% xenon- 99% nitrogen saturated to $C=20\%$ and $C=5\%$ as indicated by the curves. The bounds are not theoretical calculations.

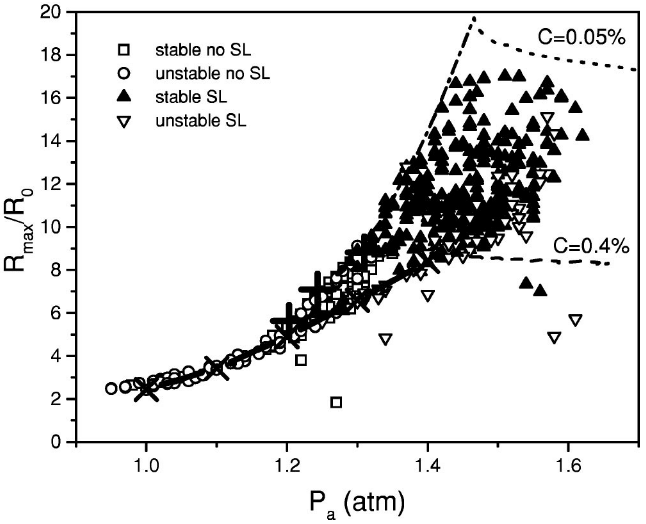

FIG. 7. Expansion ratio diagram with data points from numerous experimental runs at an assortment of gas saturations. ER curves calculated from their respective diffusive equilibrium curves are shown for $C=0.4\%$ (dashed) and $C=0.05\%$ (dotted). Also plotted is the ER for the 10% air dissociation equilibrium (solid with +), the $n=4$ shape threshold (solid with ×), and the point on a fixed C curve where the slope equals infinity (dash dotted).

In general, the higher intensities for a fixed P_a correspond to higher noble gas concentrations, which is illustrated by the $C=5\%$ and $C=20\%$ xenon curves in Fig. 6. Higher gas concentrations also cause the bubble to reach the shape threshold and thus the light extinction threshold at a lower P_a. This results in the maximum possible light intensity decreasing somewhat for lower values of C as P_a gets above ≈ 1.5 atm. The turn-on P_a of light emission also varies depending on the noble gas concentration, resulting in a fairly wide range of P_a $(1.25-1.4$ atm) where the SL intensity is nearly zero.

F. Overall ER vs P_a diagram

Figure 7 shows the ER vs P_a diagram for all the data. At $P_a<1.2$ atm the bubble is unstable and nonluminescing (open circles) and appears to follow the path of the $n=4$ shape threshold curve (solid with ×) quite closely. Lower order modes would show similar agreement since all the curves lie close together in parameter space at low P_a. From $1.2<P_a<1.3$ atm the bubble reaches a stable dissociation equilibrium as the diatomic gases within it begin to dissociate (open squares). The stable non-SL data points agree fairly well with the dissociation equilibrium for 10% air (solid with +) for $P_a<1.25$ atm. The actual path of stable non-SL seems to vary, depending on the amount of nitrogen in the fluid, with the largest deviations occurring as P_a increases. The net effect is that all the stable non-SL points sweep out a cone shaped region between the shape threshold and some upper bound for the stable dissociation equilibrium [8]. For $1.3<P_a<1.6$ atm a large region of stable SL exists (solid triangles) that is bounded in much the same way as were the stable SL points in Fig. 5.

The upper and lower ER limits for stable SL are roughly bounded by the ER curves corresponding to $C=0.4\%$ (dashed) and $C=0.05\%$ (dotted). Thus the lowest ERs observed here for SL were ≈ 8 and the highest ERs were ≈ 17. The left side of the stable region is bounded by the dissociation equilibrium and the ER calculated at the point on a fixed C curve where the slope equals infinity (dash dotted). This curve also represents SL turn-on. The lower side of the stable SL region appears to be bounded by the $n=4$ shape threshold (solid with ×). The shape threshold acts as the cut off for SL or as the path that unstable SL bubbles follow (open triangles) [5,25].

The overall region of stable non-SL and stable SL map out the ''dissolution island'' first observed by Holt and Gaitan [4]. Interestingly, the features of this diagram are much smoother than those in Fig. 5. The data starts at low P_a on a single line and then smoothly open up to form a funnel shape as P_a increases. The ER diagram may in fact be a more useful way to view data since it also gives some information about the strength of collapse.

IV. CONCLUSIONS

Experimental phase diagram data have been presented for a series of krypton-nitrogen gas saturations, and for a large collection of data from assorted noble gas-nitrogen mixtures at a variety of saturations. The krypton data showed that DH can be used to predict paths in parameter space that a stable bubble will travel along. The overall collection of data showed that DH can be used to predict regions of bubble behavior in parameter space.

The overall collection of data also represents a complete mapping of the parameter space of SL at a single frequency. The results build upon and confirm the very important experiments of Holt and Gaitan [4], who first noted the regions of stability in parameter space for SL and non-SL bubbles. In fact, the SL data points in Fig. 5 map out the ''dissolution island'' first noted by Holt and Gaitan, which was one of the key observations in the development of DH.

An interesting feature of the R_o-P_a phase diagram was the apparent agreement between the upper bound of SL and the $n=4$ shape threshold calculated by Wu. The observation of the stability boundary at the $n=4$ mode for higher P_a was surprising, because it was previously assumed that the $n=2$ mode, the first to set in [26], was responsible for unstable SL. In fact, occasionally we saw signs of the $n=2$ mode while the bubble was luminescing without seeing any signs of ''dancing'' behavior [1,4,17] or extinction [22]. Holt and Gaitan [4] and Tian *et al.* [14] have made similar observations, but for bubbles that were *not* luminescing. An understanding of the mechanical means by which the $n=4$ mode may contribute to extinction or unstable SL, if at all, and over what time scale, is still lacking.

For each phase diagram used to test DH, the relative light intensity of SL was also recorded. In general, the brightest bubbles occurred at the smallest ERs (≈ 8), and the faintest bubbles occurred at the highest ERs (≈ 17). The light intensity for helium, neon, and argon all appeared similar for a fixed value of P_a. Differences in the maximum light intensity for each of these noble gases were not large enough to make any definitive conclusions. Krypton and xenon, however, were distinctly brighter at a fixed P_a, with xenon being the brightest noble gas of all, as was first noted by Hiller *et al.* [2]. For both xenon and krypton the light intensity increased as the noble gas concentration was increased for a fixed P_a. Perhaps with more sensitive light detection equipment, similar trends would have been observed for the other noble gases.

ACKNOWLEDGMENTS

We wish to acknowledge many valuable discussions with G. Holt, T. Matula, S. Hilgenfeldt, and R. Roy. We also wish to thank C. Wu, T. Arlman, and Y. Hao for sharing results of their numerical calculations.

[1] D. F. Gaitan, L. A. Crum, C. C. Church, and R. A. Roy, J. Acoust. Soc. Am. **91**, 3166 (1992).

[2] R. Hiller, K. Weninger, S. J. Putterman, and B. P. Barber, Science **266**, 248 (1994).

[3] R. Löfstedt, K. Weninger, S. Putterman, and B. P. Barber, Phys. Rev. E **51**, 4400 (1995).

[4] R. G. Holt and D. F. Gaitan, Phys. Rev. Lett. **77**, 3791 (1996).

[5] S. Hilgenfeldt, D. Lohse, and M. P. Brenner, Phys. Fluids **8**, 2808 (1996).

[6] D. Lohse *et al.*, Phys. Rev. Lett. **78**, 1359 (1997); D. Lohse and S. Hilgenfeldt, J. Chem. Phys. **107**, 6986 (1997).

[7] S. Hilgenfeldt, S. Grossmann, and D. Lohse, Nature (London) **398**, 402 (1999).

[8] D. F. Gaitan and R. G. Holt, Phys. Rev. E **59**, 5495 (1999).

[9] J. A. Ketterling and R. E. Apfel, Phys. Rev. Lett. **81**, 4991 (1998).

[10] J. A. Ketterling, Ph.D. dissertation, Yale University, 1999 (unpublished).

[11] B. P. Barber *et al.*, Phys. Rep. **281**, 66 (1997).

[12] L. Kondić, J. I. Gersten, and C. Yuan, Phys. Rev. E **52**, 4976 (1995); W. C. Moss, D. B. Clarke, and D. A. Young, Science **276**, 1398 (1997).

[13] W. C. Moss *et al.*, Phys. Rev. E **59**, 2986 (1999).

[14] Y. Tian, J. A. Ketterling, and R. E. Apfel, J. Acoust. Soc. Am. **100**, 3976 (1996).

[15] R. G. Holt, D. F. Gaitan, A. A. Atchley, and J. Holzfuss, Phys. Rev. Lett. **72**, 1376 (1994).

[16] T. J. Matula and R. A. Roy, Ultrason. Sonochem. **4**, 61 (1997); T. J. Matula, R. A. Roy, and P. D. Mourad, J. Acoust. Soc. Am. **101**, 1994 (1997).

[17] B. P. Barber *et al.*, Phys. Rev. Lett. **72**, 1380 (1994).

[18] C. C. Wu and P. H. Roberts, Phys. Lett. A **250**, 131 (1998).

[19] A. Prosperetti and Y. Hao, Philos. Trans. R. Soc. London, Ser. A **357**, 203 (1999).

[20] A. Eller and H. G. Flynn, J. Acoust. Soc. Am. **37**, 493 (1965); M. M. Fyrillas and A. J. Szeri, J. Fluid Mech. **277**, 381 (1994).

[21] T. Arlman, S. Hilgenfeldt, and D. Lohse (unpublished). The curve is actually calculated for a mixture of 1% xenon and 99% nitrogen. However, since the nitrogen mainly influences the location of the curve, the curve for krypton would show little difference. The calculation includes the effect of water vapor on the internal temperature of the bubble.

[22] S. M. Cordry, Ph.D. dissertation, University of Mississippi, 1995 (unpublished).

[23] K. Yasui, J. Phys. Soc. Jpn. **66**, 2911 (1997); B. D. Storey and A. J. Szeri, Proc. R. Soc. London, Ser. A (to be published).

[24] C. C. Wu (unpublished). Calculations of the $n=2$ mode by Wu and Roberts are in close agreement to similar calculations by Hilgenfeldt (unpublished) [5] and Hao (unpublished) [19].

[25] J. A. Ketterling and R. E. Apfel, J. Acoust. Soc. Am. **107**, L13 (2000).

[26] M. P. Brenner, D. Lohse, and T. F. Dupont, Phys. Rev. Lett. **75**, 954 (1995).